Two- and three-body forces in the interaction of He atoms with Xe overlayers adsorbed on (0001) graphite

R. A. Aziz
Department of Physics, University of Waterloo, Waterloo, Ontario N2L 3G1, Canada

U. Buck
Max-Planck Institut für Strömungsforschung, Bunsenstrasse 10, 3400-Göttingen, Federal Republic of Germany

H. Jónsson
Chemistry Department, University of Washington, Seattle, Washington 98195

J.-C. Ruiz-Suárez[a)]
Department of Physics, University of Waterloo, Waterloo, Ontario N2L 3G1, Canada

B. Schmidt
Max-Planck Institut für Strömungsforschung, Bunsenstrasse 10, 3400-Göttingen, Federal Republic of Germany

G. Scoles
Department of Chemistry, Princeton University, Princeton, New Jersey 08544-1009

M. J. Slaman
Department of Physics, University of Waterloo, Waterloo, Ontario N2L 3G1, Canada

J. Xu[b)]
Department of Chemistry, Princeton University, Princeton, New Jersey 08544-1009

(Received 10 July 1989; accepted 4 August 1989)

In order to address the problem of three-body interactions in gas–surface scattering, we considered the collision of a He atom with the (0001) surface of graphite coated by a monolayer of Xe. To eliminate the uncertainties connected with errors in the two-body He–Xe interaction, we determined the latter by crossed-beam differential collision cross-section measurements performed at two energies (67.2 and 22.35 meV). These scattering data together with room-temperature bulk diffusion data are then fitted with a Hartree–Fock–dispersion–type function to yield an interaction potential that explains most of the properties of this system within the experimental errors and represents an improvement on previously published He–Xe potentials. Helium diffraction measurements are then carried out from the Xe overlayer and the dependence of the specular intensity from the angle of incidence is carefully determined. Further, a He–surface potential is constructed by adding together the following terms: (1) the He–Xe pairwise sum, (2) the long-range He–(0001)C interaction, (3) the three-body contribution generated by the Axilrod–Teller–Muto term, (4) the so-called surface-mediated three-body interaction He–Xe–(0001)C first considered by A. D. McLachlan [Mol. Phys. 7, 381 (1964)], and finally (5) a small correction which is meant to take into account the nonstationary nature of the surface. Using this potential, well-converged close-coupling scattering calculations are carried out, and their results compared with the data. In general, good agreement is obtained. The agreement can, however, be improved by (a) an increase of about 30% in the contribution of three-body forces, (b) the lowering of the He–graphite long-range attraction coefficient by about 15%, or (c) a reduction of the two-body interaction well depth of 1.6% (the experimental error) together with any combination of the factors under (a) and (b) reduced by an adequate amount. Elimination of the contribution of the graphite surface by studying Xe multilayers is hindered by the uncertainties in the "thermal correction" [point (5) above] which, due to the multilayer increased "softness," becomes an appreciable source of uncertainty.

INTRODUCTION

During the last decade our knowledge and understanding of the physisorption of gases on single-crystal surfaces has increased substantially. Thermodynamic,[1] scattering,[2] and spectroscopic[3] techniques have been used to obtain a large body of information on the structure and stability of these quasi-two-dimensional phases.[4] Most of the structural information gathered so far has been obtained by electron,[5] neutron,[6] x-ray,[7] or atom scattering.[8]

The reasons behind all of this activity are both of fundamental and applied nature. First of all, we note that, despite the efforts towards understanding wetting phenomena in chemical, engineering, and biological processes, the condi-

[a)] Present address: Centro de Ciencias de la Atmósfera, Circuito Exterior, Ciudad Universitaria, C.P. 04510, Mexico.
[b)] Present address: Brookhaven National Laboratory, Physics Department, Bldg. 510B, Upton, NY 11973.

tions that determine whether one material will spread over the surface of another are not yet well understood in microscopic terms.[9] Most of the work to date[10,11] has emphasized the relative strengths of the adsorbate–substrate and the adsorbate–adsorbate interactions, neglecting the role played by the size and the shape of the adsorbate molecules and the size and relative locations of the atoms forming the adsorbing surface.

Secondly, the ever increasing list of quasi-two-dimensional phase-transition phenomena occurring in physisorbed overlayers has been a strong pole of attraction for people interested in modern statistical mechanics and computer-simulation methods.

The third fundamental reason for studying overlayers, and one of the main motivations for the present work, stems from the fact that their interaction with impinging atoms of molecules can be calculated with a much higher degree of precision than in the case of atom or molecule bare–solid interactions. Indeed, although quantitative or semiquantitative agreement between calculated and measured scattered intensities is known for a few cases[12] atom–bare-surface interactions are still known with insufficient precision.[13] On the other hand, atom–overlayer potentials, obtained by summation over pairwise interactions (with or without the assumption of additivity[14]) combined with quantitative close-coupling scattering calculations, provide better models and can lead to an improved knowledge on the nature of three-body forces in condensed systems.

Finally, we should note that overlayers are also the subject of intense investigation in many areas of applied science and technology, perhaps the most important of these being the field of epitaxial growth of thin films and layered solids. These very important technological materials can be grown by several methods such as molecular-beam epitaxy, chemical vapor deposition, sputter deposition, and laser-assisted processing. In all cases a thorough understanding of the mechanisms of growth and stabilization of the films is essential for the production of state-of-the-art devices such as electronic components, solid-state lasers, transducers, etc. However, most technologically important films contain a variety of physical and chemical interactions and therefore are very difficult to study theoretically. Physisorbed films, with their better known interactions, provide us with extremely useful models for the study of dynamics at interfaces. For instance, a knowledge of the factors that determine interlayer mixing is obviously important for setting the conditions for growing those layered structures with the sharp interlayer boundaries that are required for optimum device performance.

The first quantitative comparisons between theory and experiment in atomic scattering from overlayers were carried out by Ellis *et al.*[8(c)] These authors studied the interaction of H atoms with Xe and Kr monolayers physisorbed onto the basal plane of graphite. In the analysis of the data, two-body potentials determined by gas-phase experiments were used to construct, via pairwise additivity, atom-overlayer potentials. To these potentials the long-range van der Waals interaction with the graphite substrate was added. Good agreement between theoretical intensities calculated via a close-coupling algorithm and the experimental data was obtained. It was also shown that the calculated intensities were very sensitive to the details of the potential used.

Shortly after the experiments of Ellis *et al.*, selective adsorption measurements of He atoms from Xe/C(0001) were reported by Bracco *et al.*[15(a)] Close-coupling calculations for this system were carried out by Hutson and Schwartz.[15(b)] Due to the substantially larger monochromaticity of He beams (vs those made of atomic hydrogen) the comparisons between experiments and theory were more significant in this case. One of the main objectives of Hutson and Schwartz's calculations was to learn about the effects of many-body interactions in the gas–surface scattering process. They concluded that the effect on the calculated intensities of the nonadditive triple-dipole interactions were of the same order as those produced by the uncertainties of the He–graphite and He–adatom interaction potentials. Another conclusion was that the sensitivity of the data to changes in the potential is strongly dependent on the energy of the incident beam. In fact, at the incident energy of 22 meV (the energy used by Bracco and co-workers) two slightly different pair potentials gave similar scattering patterns. On the other hand, the predicted intensities for these two potentials showed strong differences at a lower incident energy (9.36 meV).

More recently, selective adsorption measurements of He atoms from commensurate Kr monolayers adsorbed on C(0001) were carried out by Larese *et al.*[8(h)] The aim of that work was to study a system in which the He–adatom pair potential was better known, removing one of the uncertainties in the evaluation of the nonadditive interactions. A precise estimate for the energy levels of the He–Kr/graphite system was obtained by Jónsson and Weare,[16(a),16(b)] who compared the results of close-coupling calculations with the resonant patterns measured in Ref. 8(b). The potential used in the calculations was constructed by summing over the He–Kr pair interactions and the He–graphite interaction. Three-body corrections were added calculating not only the triple-dipole interaction but also the correction due to the repulsive exchange interaction.[16(b)] At first the calculated energy levels did not agree with the "experimental" ones.[16(a)] However, the discrepancy was resolved when the He–graphite interaction was redetermined independently by two groups[16(c),16(d)] and the previously reported measurements were found to be in error. With the new He–graphite interaction the agreement produced by the theoretical many-body correction could be considered very good.[16(b)]

Since for He–Xe/graphite the contributions to the potential of the many-body interactions are larger, we decided to undertake a comprehensive study of this system based on the independent redetermination of the He–Xe two-body potential and the use, in the He–surface scattering experiments, of very low beam energies. The former goal was achieved by remeasuring the He–Xe differential collision cross section at the Max-Planck Institute in Göttingen and checking the results by calculating several bulk gas-phase properties while the gas–surface scattering experiments made use of the low-energy He beam diffractometer built at the University of Waterloo and presently located at Prince-

ton. The choice of operating the He beam at lower energies is dictated by several reasons. First, the scattering of low-energy atoms is more sensitive to the fine details of the gas–surface interaction potential.[15(b)] Secondly, the close-coupling scattering calculations needed to analyze the data become less expensive at lower energies since fewer channels are needed to obtain convergence. Finally, the use of low-energy beams gives rise to substantially less inelastic scattering so that the analysis of the elastic intensities can be more reliably extracted from "total" scattering experiments such as ours.

Quite recently two series of impressive experiments have appeared in the literature involving He scattering from Xe overlayers physisorbed on metals. In the first, carried out at the Kernforschungsanlage at Jülich, the structure and dynamics of Kr and Xe overlayers on (111) Pt has been determined.[17] However, so far, no close-coupling calculations have been carried out on these systems, and therefore no information has been extracted on the He–rare-gas overlayer interaction potential. The second series of experiments has been carried out at the University of Chicago and has consisted of elastic and inelastic studies of ordered noble-gas (Ar, Kr, Xe) overlayers physisorbed on Ag(111).[18] The last of the University of Chicago papers, in which the elastic scattering experiments are described, contains close-coupling calculations and logically concludes that three-body terms are needed in the interactions and that "further refinements in He–(heavy-rare-gas) pair potentials may be in order."

Our paper is organized as follows. In Sec. II we describe the atom–surface scattering apparatus and results. Section III describes the determination of a new, improved two-body He–Xe interaction. This section is subdivided into four parts. In Sec. III A experimental information is given on the crossed-beam scattering apparatus used in the measurements and the results of the same, while in Sec. III B the data analysis and fitting procedures are described. In Sec. III C the results are discussed and comparison is made with the potentials previously published in the literature. Finally, in Sec. III D the improved He–Xe potential is tested in its ability to predict other properties of this system that depend exclusively on two-body collisions such as virial coefficient, viscosity, thermal diffusion, etc. In Sec. IV we outline the way in which atom–surface potentials are calculated, the way in which the close-coupling scattering calculations are carried out, and the results obtained comparing our experimental data with the results of calculations that utilize both new and old two-body potentials. Finally, some conclusions are drawn and recommendations for future work are made.

II. ATOM–SURFACE SCATTERING: APPARATUS AND RESULTS

Our experiments were carried out with a molecular-beam apparatus[19] which is a modification of the one used in previous work.[20] Basically, it consists of two stainless-steel chambers (see Fig. 1). The first of these, pumped by an unbaffled VHS-400 oil diffusion pump, contains a variable en-

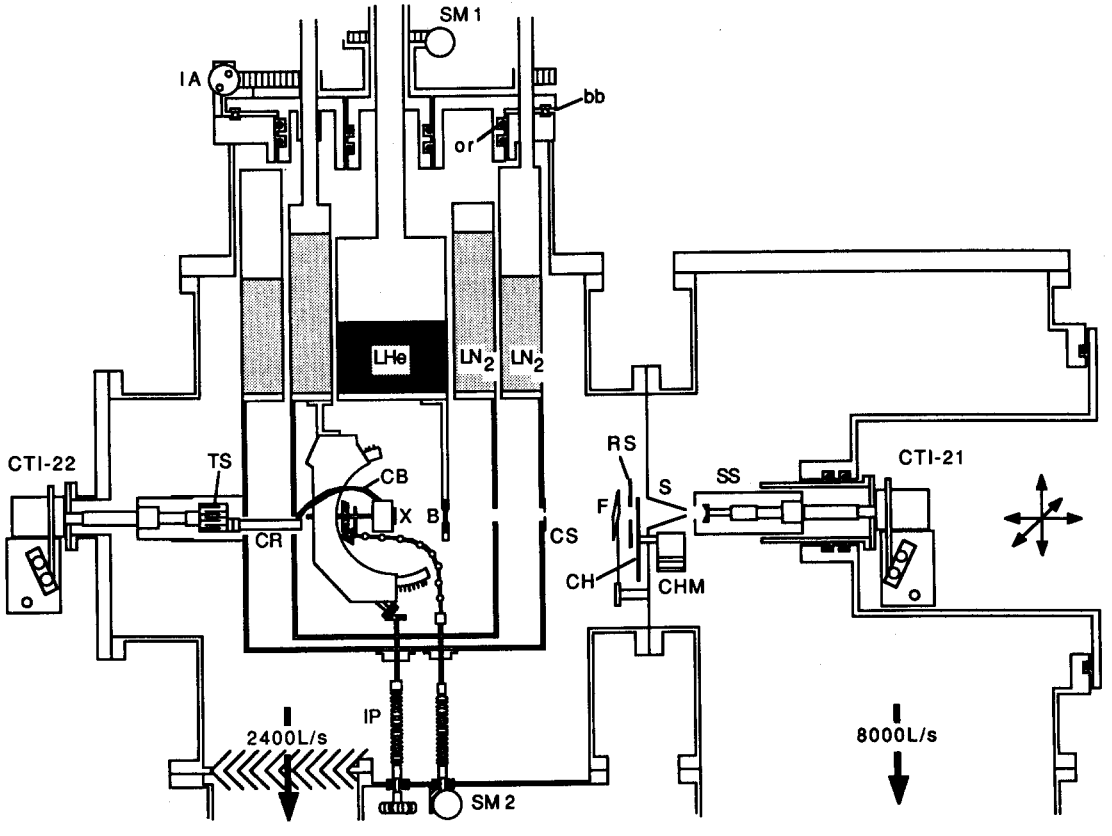

FIG. 1. Schematic cross-sectional view of the surface scattering apparatus. B, bolometer; CB, copper braid; CH, chopper; CHM, chopper motor; CR, copper rod; CS, collimating slit; CTI-21, cold head 2; CTI-22, cold head 1; F, flag; IA, incident angle control; IP, in-plane angle control; RS, radiation shield; S, skimmer; SM 1, stepping motor for bolometer position control; SM 2, stepping motor for azimuthal angle control; SS, supersonic helium source; TS, thermal switch; X, crystal; bb, ball bearings; or o-rings.

ergy He atom supersonic source. The second chamber is pumped by a water baffled VHS-250 oil diffusion pump via an auxiliary chamber (not shown in Fig. 1) which contains a 160 K cold trap. The second chamber houses a liquid-He cryostat surrounded by two liquid-N_2 shields. The detector is attached at the bottom of the liquid-He cryostat while the crystal manipulator is anchored at the bottom of the inner liquid-N_2 reservoir. Under zero beam pressure conditions the measured vacuum in the scattering chamber, outside the 77 K shields, is approximately 8×10^{-8} Torr. The vacuum inside the 77 K shroud has never been measured but the partial pressures for all gases but He and H_2 are estimated to be substantially better than 10^{-10} Torr.

The He beam source is a modified version of the source described in Ref. 19. The nozzel is a 20 μm molybdenum electron-microscope aperture cooled by a commercial CTI model 22 cryocooler. The cryocooler is physically mounted onto the inside face of a cylindrically shaped flange which extends into the middle of the source chamber (see Fig. 1). The flange is capable of small displacements in the X, Y, and Z directions. With these movements the position of the nozzle is optimized in front of a 290 μm diam skimmer. After the skimmer the beam passes a slotted wheel chopper, a coarse collimator, and a beam defining collimator whose dimensions are 0.2×2.0 mm^2 (the longer dimension being in the vertical direction). The distance between the nozzle and the beam defining collimator (C_2) is 200 mm. With the help of a nichrome heater, a semiconductor sensor, and an electronic feedback system, the source can be maintained at any temperature between 30 and 300 K with a stability of 0.5 K. The source produces intense and well-collimated He beams with a dispersion in velocity $\Delta v/v$ better than 2%, as estimated by the width of the diffraction peaks as compared to the width of the specular beam.

The crystal manipulator allows the rotation of the crystal around three mutually perpendicular directions allowing for changes in the incident angle θ_i, the azimuthal angle ϕ, and the out-of-plane angle ψ. The crystal is normally kept at temperatures about 500 K by means of a tungsten heater. During experiments, low crystal temperatures are obtained with the help of a cooling system which uses a second closed-cycle refrigerator unit. The main feature of this cooling system is a thermal switch, operated with He gas, which provides a good thermal contact when the sample is cooled and thermal isolation when it is heated and He is pumped out of the switch. The thermal switch is fastened to the coldest stage of the cryogenic head. In this way crystal temperatures of 35 K have been achieved.

The detector used is a semiconductor bolometer 3.0 mm high and 0.3 mm wide attached to a liquid-He cryostat that can rotate around its vertical axis. In this way, the bolometer can sweep the horizontal scattering plane. The cryostat has a capacity of 1.5 liter and an average operating time of 18 h. The operating temperature of the detector is ~1.7 K, which is obtained by pumping on the liquid-He cryostat with a rotary pump. The responsivity of the bolometer is 3×10^5 V W^{-1} and a noise-equivalent power of at least 10^{-12} W Hz$^{-1/2}$. A standard lock-in amplifier and a microcomputer take care of signal amplification, integration, and storage. The formation of the Xe layers on the graphite basal plane was followed by monitoring the specular reflection of the He beam and is illustrated in Fig. 2. The first drop in intensity shown in the figure corresponds to the formation of the first layer which is completed not long after the minimum around 77 K. The consequent increase in specular intensity is due to the decrease of inelastic scattering. The second layer forms around 60 K followed soon after (at 57 K) by the formation of the third. After that, the changes in specular intensity due to further layer formations are too small to compensate for increases due to the decrease of the inelastic scattering. When, as it was the case in the great majority of the runs, scattering from the first layer is to be measured, the Xe flux is stopped before the formation of the second layer and the sample is cooled down to 40 K.

Figure 3 shows a typical He–Xe/C(0001) diffraction scan. The angular positions of the diffraction peaks give a lattice parameter of 4.30 Å (the experimental error is $\pm$ 0.02 Å). Therefore, the lattice mismatch with the graphite substrate is very near zero (twice the experimental error), while the rotation of the $(\sqrt{3}\times\sqrt{3})$ structure is (within experimental errors) 30°. It should be noted that the width of the specular beam is wider than that of the main beam, which implies the existence of a fair amount of defects in the layers and the grapite substrate. Figure 4 shows the result of a scan of experimental intensities of the specular He beam as a function of the incident angle θ_i. The energy of the beam was 8.80 meV ($k=4.10$ Å^{-1}) and the azimuth was $\phi=0$. The specular intensities, which are normalized to the He primary beam, were obtained either by scanning through ϕ for several values of θ_i and identifying $\phi=0$ as the point about which the scans showed reflection symmetry, or by ϕ optimization carried out on a diffraction peak. Without this precaution, polar scans of this type are very often found to be in error. Figure 5 shows a set of azimuthal scans for several incident angles. In both polar and azimuthal scans, sharp minima and maxima are observed. These are associated with scattering resonances, called selective adsorption, which reflect the presence of bound states of the He atom in the gas–surface potential.

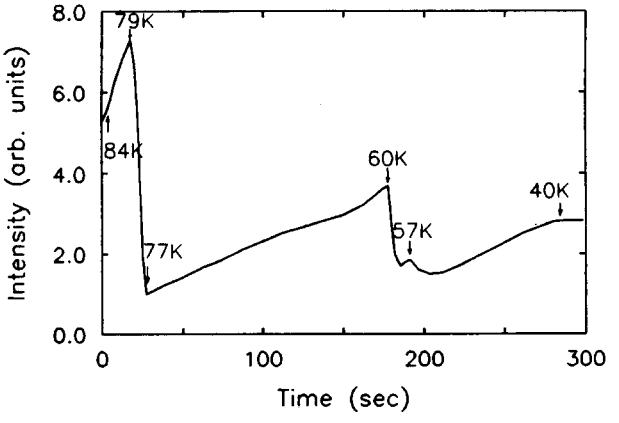

FIG. 2. The formation of Xe layers on (0001) graphite monitored by the behavior of the specular He beam intensity.

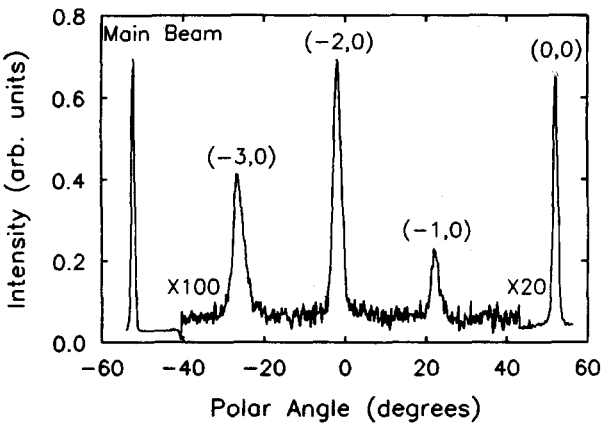

FIG. 3. Typical diffraction data for He scattered by a Xe layer adsorbed on (0001) graphite crystal. Azimuth $\phi = 0°$ (with respect to the Xe lattice). Incident energy: $E_i = 8.80$ meV. Incident angle: $\theta_i = 52.0°$.

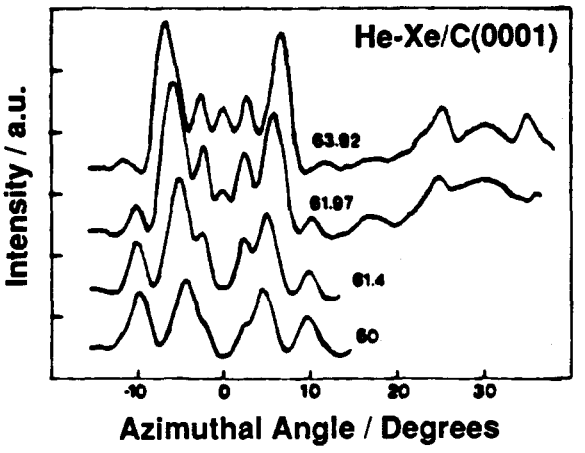

FIG. 5. Azimuthal scans for He–Xe/(0001)C at $E_i = 8.80$ meV at several values of the angle of incidence θ_i.

III. A NEW, IMPROVED, TWO-BODY POTENTIAL FOR He–Xe

A. Experimental results

Differential cross-section measurements of He–Xe at relative energies $E = 67.20$ meV and $E = 22.35$ meV were carried out in a high-resolution crossed molecular-beam machine which has been described elsewhere.[21]

The two rare-gas beams are generated as supersonic beams in two differentially pumped source chambers and are crossed at 90°. The scattered He atoms were detected at $m = 4$ amu with a triply differentially pumped detector that rotates in the plane of the two beams. It consists of an electron-bombardment ionizer, a quadrupole mass spectrometer, and a particle multiplier operated at a pressure of some 10^{-10} mbar.

To vary the collision energy, the primary beam source can be cooled to liquid-nitrogen temperatures. The most probable beam velocities and velocity distributions are measured by time-of-flight (TOF) analysis using the pseudorandom chopping technique with a flight path of 484 mm. The optimized operating conditions for the beams are listed in Table I. The measured cross sections are corrected for calibration errors of the angular scan to an accuracy of better than $\pm 0.03°$ and for the v'^{-1} dependence of the final velocity due to the number density detector. The results are presented in Fig. 6. Both cross sections are dominated by diffraction oscillations which are very pronounced for the low-temperature data. Note that the first oscillation appears only as a shoulder, a reminiscence of the existence of a rainbow in this angular region. To compare the measured angular distribution with calculations, the latter have to be transformed from the center-of-mass (CM) system to the lab system and averaged over the experimental angular and velocity distributions. The algorithm used is described in detail elsewhere.[22,23] Only the characteristic values of the distribution functions are given here, calculated with a Monte Carlo technique based on the data of Table I. The full width at half maximum of the relative velocity is $\Delta g/g = 0.034$, for the low-temperature, and 0.065, for the room-temperature data. The width of the CM angular distribution is slightly angular dependent and is given by the average values $\Delta = 1.06°$ and $\Delta = 1.08°$, respectively.

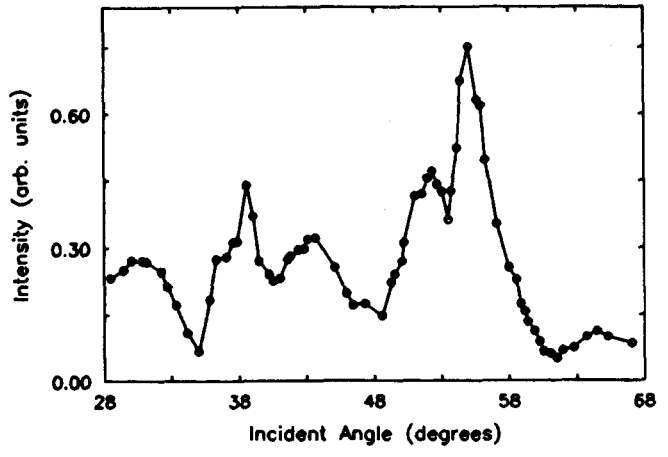

FIG. 4. Polar scan for He–Xe/(0001)C along the $\phi = 0°$ azimuth. $E_i = 8.80$ meV. $T_{sample} = 40$ K.

B. Analysis

Because of the high resolution of the cross-section data, the cross-section features and their relation to the interaction potential, can be briefly described as follows.[22]

(i) The angular positions of the diffraction oscillations establish the point (σ) at which the potential goes through zero, to a precision of better than 1%.

TABLE I. Beam operating conditions.

Gas	He	Xe	He	Xe
Temperature	room	room	liquid N_2	room
Nozzle diameter (μm)	30	200	30	200
Pressure (bar)	10	0.4	12	0.3
Peak velocity (ms^{-1})	1802	308.7	1009	306.7
Speed ratio	22.6	18.7	43.5	21.5
Angular divergence (deg)	1.04	3.0	1.04	3.0
Collision energy (meV)	67.20		22.35	

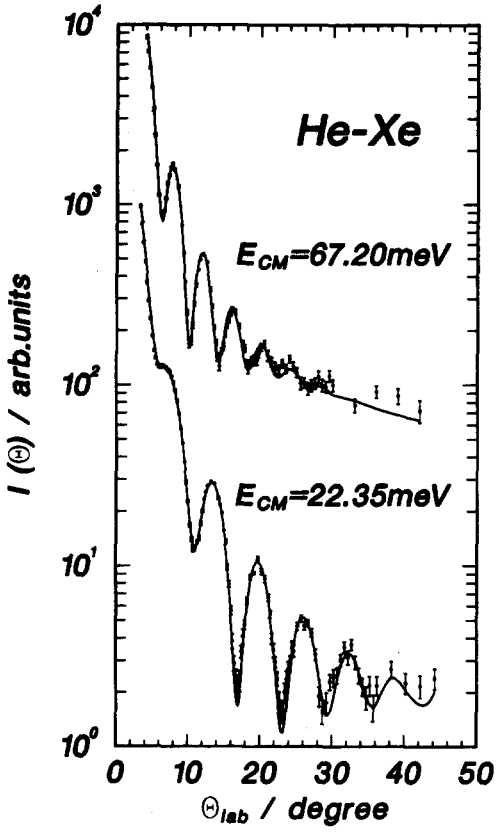

FIG. 6. Differential cross sections for HeXe at two collision energies measured as a function of the laboratory deflection angle. The curves correspond to calculations with the best-fit potential of this work. The data are shifted vertically for clarity.

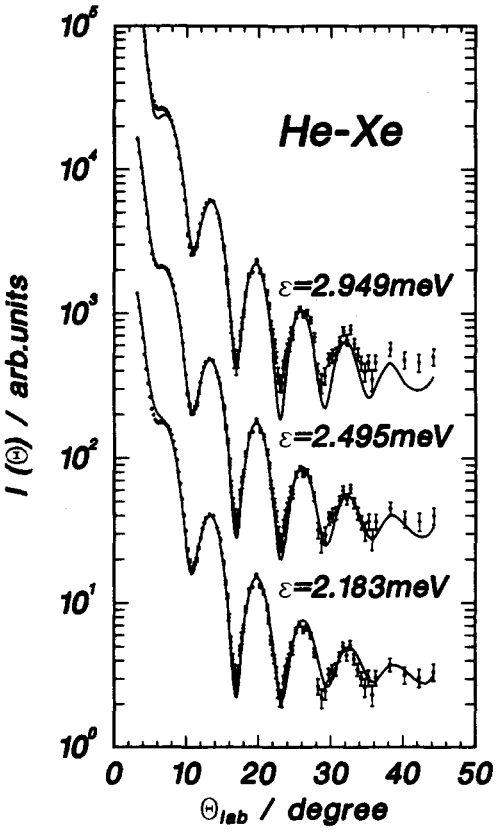

FIG. 7. Comparison of calculated differential cross sections (curves) for the HFD potential using three different well depths with the measured data at $E = 22.35$ meV. Note the sensitivity of the data to changes of ϵ, near the shoulder at small angles and at the minima at large angles.

(ii) The amplitudes of the diffraction oscillations are a measure of the potential between σ and the minimum and therefore are related to the well depth ϵ. We are *not* referring to the general falloff of the cross section[22] which is only a rough measure of ϵ, but to the amplitudes of the minima at larger angles. This was demonstrated in test calculations (carried out at constant σ for different ϵ values at the lower energy) and is shown in Fig. 7. The amplitudes of the minima at angles larger than 30° depend strongly on ϵ. It is remarkable that the extrema around 10° to 12° are not affected by these changes in ϵ so that errors in the averaging procedures can be ruled out completely, since the averaging procedures affect all the minima by the same amount.

(iii) The shoulder at small angles is only present in the low-energy data and is obviously the remnant of a rainbow. In contrast to the featues described under case (ii), this shoulder is sensitive to the attractive part of the potential near the inflection point.

All of the above results are a very strong constraint on the attractive part of the potential. To better constrain the repulsive part of the potential, the precise mixture diffusion coefficients of Arora, Robjohns, and Dunlop[24] at room temperature have been used and fitted together with the cross-section data.

The interaction is modeled by the Hartree–Fock–dispersion (HFD) potential

$$V(R) = V_{\rm HF}(R) + V_{\rm D}(R) \times F(R), \tag{1}$$

$$V_{\rm HF}(R) = A R^{\gamma} \exp(-\alpha R), \tag{2}$$

$$V_{\rm D}(R) = -\sum_{n=0}^{4} C_{2n+6} R^{-(2n+6)}, \tag{3}$$

$$F(R) = \begin{cases} \exp[-(D \cdot R_m/R - 1)^2], & R < D \cdot R_m \\ 1, & R \geqslant D \cdot R_m \end{cases}. \tag{4}$$

The C_6 dispersion coefficient is fixed at the value calculated by Kumar and Meath,[25] while the C_{10}, C_{12}, C_{14} coefficients are obtained using the recursion relations of Douketis *et al.*[26] The damping parameter is held fixed at $D \cdot R_m = 5.12$ Å. Thus, we are left with the parameters A, α, γ, and C_8 to be determined from the four measured quantities described above. The scattering calculations were carried out using quantum phase shifts and include all averaging effects.[23] The diffusion coefficient was calculated quantum mechanically, including the higher-order corrections, according to Ref. 27. The fitting procedure is based on the minimalization of the dimensionless quantity δ,

$$\delta = \left[\frac{1}{n}\sum_{i=1}^{n}\left(\frac{cX_i^{\rm expt} - X_i^{\rm calc}}{c\Delta X_i^{\rm expt}}\right)^2\right]^{1/2}, \tag{5}$$

where $X_i^{\rm expt}$ and $X_i^{\rm calc}$ are the measured and calculated data. $\Delta X_i^{\rm expt}$ is the absolute experimental error and c is a calibration constant. In the first step the best value for σ and the repulsive potential at 3 Å are determined by a fit to the differential cross sections at both energies and the diffusion coefficient, respectively. From these values A and α are calculated.

Then γ and C_8 are derived from a simultaneous fit to both cross sections.

C. Results and discussion

The resulting best-fit parameters are shown in Table II together with the parameters of the other HFD-type potentials used in this paper. The corresponding quality-of-fit parameters δ appear in Table III. The calculated differential cross sections based on the best-fit potential are shown in Fig. 6 as solid lines. The agreement between calculated and measured differential cross sections is quite satisfying. It is noted that this best-fit potential requires a small compromise between the room-temperature and the liquid-nitrogen-temperature data.

An important issue for the determination of three-body forces is the accuracy of the two-body potential. The point at which the potential goes through zero (σ) is determined to be 3.547 ± 0.015 Å. The error mainly reflects the precision to which the position of the diffraction oscillations and the relative velocity were determined. The situation for the well depth ϵ is a little more complicated. According to what we said before and Fig. 7, ϵ is determined by the amplitudes of the minima of the diffraction oscillations at larger angles for both energies and the rainbowlike shoulder which is only present at the lower energy. Figure 8 shows the results of changes of ϵ and the corresponding fits to the shoulder and the third minimum of the differential cross section at the low energy (see also Fig. 6). The best fit (with $\epsilon = 2.495$ meV) is presented in the middle. The calculation with the deeper well ($\epsilon = 2.567$ meV) reproduces the shoulder very well, but fails for the minimum. In contrast, the calculation with the shallower well ($\epsilon = 2.427$ meV) is in good agreement at the minimum but does not reproduce the shoulder. Therefore, these constraints set the error limits of the best-fit value of $\epsilon = 2.495 \pm 0.040$ meV.

The ability of a few recently proposed He–Xe potentials to fit the differential cross sections are also summarized in Table III. These potentials are displayed together with the present best-fit potential in Fig. 9. All these potentials have attractive wells between 2.35 and 2.64 meV and zero crossings within 0.03 Å. At this point it is obvious that we are dealing with rather small differences. The analysis of the atom–overlayer scattering measurements does indeed require higher precision than ever before.

TABLE III. Interatomic He–Xe potentials and quality of fit parameters.

	d(DCS,LN)[a]	δ(DCS,RT)[b]
HFD-1 (Ref. 28)	1.43	0.79
MS (Ref. 28)	1.37	1.16
DK (Ref. 29)	0.86	1.53
HFD-fit (this work)	0.86	1.07
HFD-B2 (this work)	0.99	1.00

[a] Differential cross section at liquid N_2 temperature.
[b] Differential cross section at room temperature.

With respect to their ability to fit the present differential collision cross-section data, the potentials reported previously by Smith *et al.*[28] behave as follows. The HFD-1 potential (also obtained from scattering data) has a slightly too small σ and the outer attractive wall shifted towards small distances, while the σ of the MS potential (obtained from fitting bulk properties) is a little too large and its ϵ too shallow. The potential of Danielson and Keil (DK),[29] which is fitted to room-temperature differential cross sections, virial coefficients, and viscosities, has a too large σ and a well depth and long-range attraction which are too deep.

D. Information from the analysis of bulk properties

1. Transport data

All transport data are calculated quantum mechanically using Chapman–Cowling expressions.

(a) *Viscosity.* The current potential predicts the first-order interaction viscosity of Najafi, Mason, and Kestin[27] over the temperature range from 300 to 1000 K (estimated error: $\pm 1\%$) to better than $\pm 0.4\%$. However, the interaction viscosity is not an actual experimental value and is in fact extracted from the measured mixture and pure viscos-

TABLE II. Parameters of HFD-type two-body potentials used in this paper.

Pair potential	MS[a]	HFD-1[a]	DK[b]	HFD-B[c]	HFD-fit[d]
A (meV)		8.116 57E6	2.953E6	2.483 744E5	5.3864E6
α (Å^{-1})		3.93	3.422	1.886 06	2.567 79
β (Å^{-2})		0.0	0.0	−0.315 35	0.0
γ		0.0	0.0	0.0	−3.0
D		5.0304	5.12	6.5059	5.12
C_6		1.101 4E4	1.168E4	1.179 179E4	1.168E4
C_8		5.676 55E4	9.360E4	9.537 173E5	8.542 55E4
C_{10}		3.347 613E5	9.1933E5	6.727 437 9E5	7.653 64E5
C_{12}		0.0	1.1371E7	0.0	8.635 317E6
C_{14}		0.0	1.7271E8	0.0	1.196 250 36E8
E_{min} (meV)	−2.361	−2.447	−2.638	−2.495	−2.495
R_{min} (Å)	3.980	3.930	3.997	3.961	3.975
σ (Å)	3.555	3.531	3.565	3.547	3.547

[a] Reference 28.
[b] Reference 29.
[c] Compromise potential derived in Sec. III D 4.
[d] Best-fit potential derived in Sec. III B.

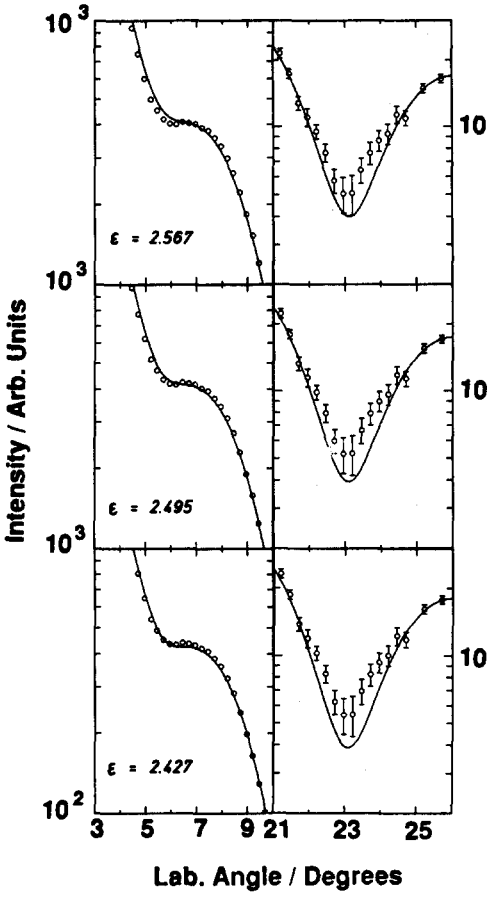

FIG. 8. Enlarged sections of the differential cross section at $E = 22.35$ meV near the shoulder at small angles and the third minimum. The solid lines are calculations based on the HFD potential for different well depths: $\epsilon = 2.567$ meV (upper panel), $\epsilon = 2.495$ meV (best fit, middle panel), $\epsilon = 2.427$ meV (lower panel).

ities using first-order Chapman–Cowling expressions for $[\eta_{\text{mix}}]_1$. While there is some error compensation involved, errors of at least several parts per thousand are quite possible.[30] An independent test of the interaction would be to calculate second-order mixture viscosity including composition dependence[31] on the basis of a proposed interaction potential, together with accurate potentials for the pure system, and compare the experiment over a reasonably wide range of mixture compositions. Accurate HFD-B potentials for helium[32] and xenon[33] are available, which, in part, were fitted to the data of Vogel.[34] The accuracy of these data is high and ranges from $\pm 0.1\%$ at room temperature to $\pm 0.3\%$ at 600 K. These potentials predict the viscosity to better than $\pm 0.2\%$. Now the deviations between the predictions of these potentials and the measured viscosities for the pure gases by Kestin, Ro, and Wakeham[35] can be as high as $\sim 0.65\%$ for helium and 1.3% for xenon. Therefore, it is not unreasonable to assign an error to the mixture viscosity of $\pm 1\%$ for He–Xe. Mixture viscosities at mole fractions (0.25, 0.50, and 0.75) of the lighter species were compared with the smoothed experimental values of Kestin *et al.*[36] in the temperature range from 300 to 973 K. The present best-fit potential predicts the mixture viscosity for He–Xe at the lowest concentration of helium to better than $\pm 0.9\%$ and at the other two concentrations to better than $\pm 0.6\%$. It is

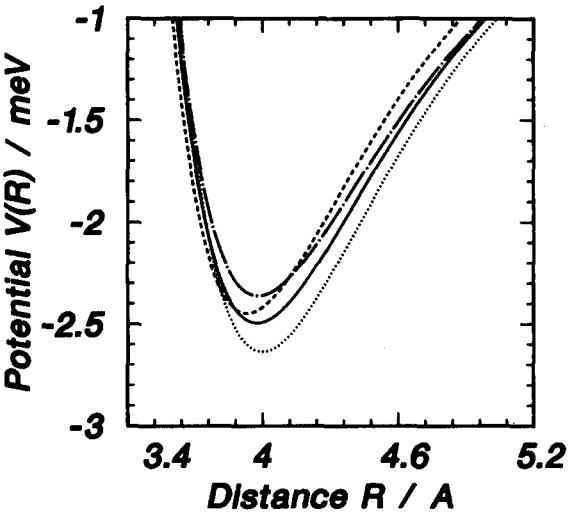

FIG. 9. He–Xe interaction potentials in the well region. Solid line: best-fit potential of this work. Dashed line: Ref. 28 (HFD-1). Dashed-dotted line: Ref. 28 (MS). Dotted line: Ref. 29 (DK).

our conviction that this potential accurately characterizes the interaction viscosity.

(b) *Diffusion.* Diffusion coefficients for helium–xenon are determined to second order including composition dependence using a three-potential calculation.[37] Quantum collision integrals are used for the helium–xenon and helium–helium interactions and classical values for the xenon–xenon interaction.

New diffusion data have been obtained by Dunlop and co-workers[38] encompassing the larger temperature range of 220–400 K (estimated error: $\pm 0.3\%$). The present potential predicts these data to within $\pm 0.23\%$. Taylor and Cain[39] measured diffusion for the helium–xenon system in the range from 350 to 1250 K with an estimated accuracy of $\pm 3\%$. The present potential predicts these data to better than $\pm 1.6\%$. Low-temperature diffusion data were measured by van Heijningen, Harpe, and Beenakker[40] in the range from 90 to 400 K. These data are estimated by Marrero and Mason[37] to have an error of $\pm 1\%$ and by Dunlop[41] to have an error of $\pm$ 1–2%. We smoothed these data using a realistic correlation function for diffusion.[42] The present potential predicts the unsmoothed data to within $\pm 2\%$ and the smoothed data to within $\pm 1\%$.

(c) *Thermal diffusion.* Trengove *et al.*[43] measured thermal diffusion factors for helium–xenon at two compositions. Independent estimates of $\pm 3\%$ accuracy have been placed on the data.[44] The data place constraints on the shape and depth of the potential well as well as on the slope of the repulsive wall. Our best-fit potential predicts these data to within the estimated error.

2. Interaction second virial coefficients

Brewer[45] measured excess virial coefficients for the helium–xenon system and determined interaction virials B_{12} in the temperature range 173–323 K using experimental values of virials for pure helium and xenon. The best-fit potential predicts these interaction virials within ± 1 cm^3/mol, except at the lowest temperature where the deviation is -1.48

cm^3/mol. Since values used for the virials of the pure components may be suspect at lower temperatures because of experimental difficulties in this temperature range, we derived revised values of B_{12} from his excess virials and calculated virials for helium and xenon based on accurate potentials.[32,33] The values so calculated differed significantly from Brewer's original values at the lower temperatures. Near room temperature, where measurement of excess virials and virials of the pure systems would be expected to be reliable, revised and original values are in close agreement. Deviations of the predicted values from the revised values at the lower temperatures are substantial, suggesting the unreliability of the low-temperature excess virials. Our suspicions are somewhat confirmed when we examine the virial correlation of Najafi, Mason, and Kestin[27] based on the law of corresponding states (LCS). Our best-fit potentials predicts the low- and high-temperature LCS values to within $\pm$ 1 cm^3/mol, but only to within about $\pm$ 2 cm^3/mol near room temperature. Interestingly, our predicted values are in close agreement with either the revised or original Brewer values near room temperature where the data are considered most reliable. Kate and Robinson[46] obtained interaction virials indirectly from solubility measurements of helium gas in solid xenon. These are sensitively dependent on reliable measurement of the vapor pressure of solid xenon. There is some question as to the reliability of the vapor-pressure data used by these authors.[47,48] Because of this possibility, we prefer to rely on the LCS virials at the lower temperatures. In summary, we can conclude that the present potential predicts acceptable virials over the whole temperature range from 120 to 773 K.

3. High repulsive region

Rol and co-workers[49] determined the high repulsive region of the potential from high-energy total collision section data. The present potential is substantially more repulsive than that of Ref. 49 (see Table IV).

4. A compromise potential

To construct a potential which removes the error in the highly repulsive wall, we chose as our model a variant of the HFD model, viz., the HFD-B form first used by Aziz and Chen:[50]

TABLE IV. Percentage differences of He–Xe potentials from the potential of Rol and co-workers (in K) in the strongly repulsive region.

R (Å)	Rol and co-workers[a]	HFD-fit	DK	HFD-B2
1.281	1 621 000	580	158	− 5.3
1.400	1 116 000	449	139	− 0.7
1.500	816 000	362	118	2.6
1.600	596 000	289	95.6	5.5
1.700	436 000	229	73.8	7.7
1.800	318 000	179	54.5	9.2
1.900	233 000	139	38.6	10.0
2.000	170 000	106	26.0	10.0
2.100	124 200	80.2	16.3	9.1
2.200	90 700	58.7	8.6	7.4
2.300	66 300	40.9	2.4	4.9
2.409	44 100	24.7	− 3.2	1.1

[a] Reference 49.

$$V(r) = \epsilon V^*(x), \tag{6}$$

where

$$V^*(x) = A^* \exp(-\alpha^* x + \beta^* x^2) - F(x) \sum_{j=0}^{2} c_{2j+6}/x^{2j+6}, \tag{7}$$

with

$$F(x) \begin{cases} = \exp[-(D/x - 1)^2], & x < D \\ = 1, & x \geqslant D \end{cases}, \tag{8}$$

where

$$x = r/r_m. \tag{9}$$

The C_6 value is chosen to be within $\pm$ 1% of the semiempirical calculation of Kumar and Meath[25] and C_8 and C_{10} are allowed to vary within the bounds proposed by Standard and Certain.[51] The well depth (ϵ) and the point (σ) at which the potential goes through zero are chosen to be identical with those of the best-fit potential. This procedure would ensure relatively good agreement with the differential collision cross-section (DCCS) data. The variables D, β, and r_m are adjusted to provide agreement with the room-temperature diffusion data of Arora, Robjohns, and Dunlop[24] and the high repulsive region determined by Rol and co-workers.[49] The parameters of the resulting potential (HFD-B2) are given in Table II. The compromise potential predicts the transport and virial data about as well as the best-fit potential and barely predicts the low-energy DCCS data, but does a good job of predicting the corresponding room-temperature data.

The predictive abilities of these potentials (HFD-fit and HFD-B2) and that of Danielson and Keil[29] (DK) are summarized in Tables V (transport properties), VI (second virial coefficients), and VII (second virial coefficient at selected temperatures).

Inspection of these tables reveals that the HFD-fit and HFD-B2 potentials are about equivalent in their ability to predict the DCCS, the various transport data, and virial coefficients. The HFD-B2 potential has, however, a more realistic wall in the highly repulsive region. The DK potential has some merit in predicting many of the transport data and second virial coefficients. Largely because it possesses a well which is too deep and a long range which is too attractive, it does not predict the DCCS data presented in this paper adequately. For the same reason, it does not predict the new diffusion data of Ref. 38 or the thermal diffusion data of Trengove *et al.*[43] within estimated error. In addition, its repulsive wall is inconsistent with the data of Rol and co-workers.[49] While the HFD-B2 potential does not predict the DCCS data quite as well as the HFD-fit potential, it is an excellent compromise potential because of its realistic high-energy wall.

IV. ATOM–SURFACE POTENTIAL FOR He–Xe/C(0001)

A. Atom–surface potential calculations

The total atom–surface interaction potential for the He–Xe/C(0001) system can be written as

TABLE V. Root-mean-square deviations for tranport properties of He–Xe for various potentials. Column (a) gives the rms deviation. Quantities in parentheses refer to rms percentage deviation. Column (b) gives the maximum ± percent deviation.

Data and reference	Temperature range (K)	Error bars (%)	HFD-fit (a)	HFD-fit (b)	HFD-B2 (a)	HFD-B2 (b)	DK (a)	DK (b)
(i) Interaction viscosity (μPa s)								
Najafi *et al.*[a]	300–1000	1.0	0.064(0.28)	−0.42 to −0.18	0.099(0.51)	−0.77 to −0.37	0.089(0.58)	−1.29 to +0.23
(ii) Mixture viscosity (μPa s)								
Kestin *et al.*[b]								
($x_{He}=0.25$)	300–973	1.0	0.300(0.62)	−0.78 to +0.43	0.297(0.62)	−0.80 to +0.48	0.281(0.60)	−0.61 to +0.32
($x_{He}=0.50$)	300–973	1.0	0.186(0.40)	−0.48 to +0.47	0.177(0.39)	−0.53 to +0.38	0.145(0.34)	−0.55 to +0.26
($x_{He}=0.75$)	300–973	1.0	0.068(0.17)	−0.19 to +0.31	0.061(0.16)	−0.25 to +0.20	0.103(0.20)	−0.27 to +0.33
Diffusion (1.0134 bars) (10^{-4} m^2/s)								
Arora *et al.*[c]	277–321	0.3	0.001 50(0.28)	+0.22 to +0.31	0.000 84(0.15)	+0.11 to +0.18	0.000 37(0.07)	−0.16 to −0.01
Dunlop[d]	220–400	0.3	0.000 78(0.10)	−0.05 to +0.23	0.001 04(0.14)	−0.17 to +0.29	0.001 84(0.34)	−0.53 to +0.42
van Heijningen *et al.*[e]	169–400	1–2	0.003 59(0.99)	−0.17 to +1.95	0.003 30(0.87)	−0.27 to +1.70	0.002 82(0.74)	−0.86 to +1.09
van Heijningen *et al.* (smoothed)[e]	169–400	1.0	0.002 59(0.60)	−0.17 to +0.90	0.002 13(0.43)	−0.27 to +0.65	0.001 67(0.46)	−0.86 to +0.13
Taylor-Cain (smoothed)[f]	350–1250	3.0	0.0411(0.94)	−1.85 to +1.18	0.0257(0.90)	−0.78 to +1.40	0.0386(1.30)	−0.25 to +1.89
Thermal diffusion factor								
Trengove *et al.*[g]	300	3.0	0.0061(1.39)	−1.80 to +0.79	0.0064(1.85)	−0.22 to −2.61	0.0221(4.64)	−3.22 to −5.72

[a] Reference 27.
[b] Reference 36.
[c] Reference 24.
[d] Reference 38.
[e] Reference 40.
[f] Reference 39.
[g] Reference 43.

$$V = V_2 + V_s + V_3 + V_{3s} + V_t, \tag{10}$$

where V_2 is the pairwise sum of the He–Xe interactions and V_s denotes the interaction of the He atoms with the graphite substrate in the absence of the overlayer. The next two terms are the nonadditive, three-body triple-dipole interaction, either involving a He atom and pairs of Xe adatoms (V_3) or a pair of He and Xe atoms and the substrate (V_{3s}). Other three-body corrections, such as the correction to the repulsive exchange term (which was shown by Jónsson and Weare to be very small[16(b)]) and the higher multipole terms *DDQ*, *DQQ*, etc. (which were estimated and are discussed below) are not included in the calculation. Four-body and higher-order terms are also neglected. It should be noted that the two- and three-body terms are, in this way, calculated under the assumption that the Xe layer is rigid. However, even at very low temperatures, the adsorbed atoms undergo thermal motion. The last term in Eq. (10), V_t, is a correction to take into account this thermal effect.[52]

Being a periodic function of the surface coordinate **R**, the total potential $V(\mathbf{R},z)$ can be expanded in a Fourier series of the surface reciprocal-lattice vectors, G_{mn}:

$$V(\mathbf{R},z) = V_{00}(z) + \sum_{G_{mn}\neq 0} V_G(z)\exp(i\mathbf{G}_{mn}\cdot\mathbf{R}). \tag{11}$$

The first Fourier coefficient, $V_{00}(z)$, gives the laterally averaged gas–surface potential which determines the energy of the bound states. All the terms in Eq. (10) have been taken into account in computing the V_{00} component, while only the two-body interaction, which alone accounts for about 90% of the total energy, is included in the higher-order Fourier components since the effect of all other terms on

TABLE VI. Root-mean-square deviations for second virial coefficients of He–Xe for various potentials. Column (a) gives the rms deviation. Column (b) gives the maximum ± deviation in cm^3/mol.

Data and reference	Temperature range (K)	HFD-fit (a)	HFD-fit (b)	HFD-B2 (a)	HFD-B2 (b)	DK (a)	DK (b)
Brewer[a]	173–323	0.908	−1.48 to +0.47	0.773	−1.22 to +0.69	1.152	−1.83 to +0.28
Brewer (revised)[a]	173–323	3.247	−5.89 to +0.18	3.058	−5.61 to +0.40	3.522	−6.34 to −0.01
Najafi *et al.*[b]	120–773	1.221	+0.51 to +1.98	1.414	+0.50 to +2.18	1.026	−0.14 to +1.81
Kate-Robinson[c]	120–155	2.876	−0.46 to +4.62	3.145	−0.16 to +4.98	2.291	−1.02 to +3.75

[a] Reference 45.
[b] Reference 27.
[c] Reference 46.

TABLE VII. Deviations from experimental second virial coefficients at selected temperatures in units of cm³/mol.

Potential	Temperature (K)	Brewer data		
		Brewer[a]	Revised[a]	Najafi *et al.*[b]
HFD-fit	120	···	···	0.740
	273.15	0.473	0.183	1.867
	373.15	−0.371	−0.411	1.940
	773.15	···	···	0.506
HFD-B2	120	···	···	1.098
	273.15	0.688	0.398	2.082
	373.15	−0.182	−0.222	2.129
	773.15	···	···	0.503
DK	120	···	···	−0.136
	273.15	0.279	−0.011	1.673
	373.15	−0.524	−0.564	1.787
	773.15	···	···	0.276

[a] Reference 45.
[b] Reference 27.

these components is negligibly small.

The sum of the two-body pair interactions over the atoms forming the layer is carried out by the analytical procedure described by Steele.[53] This procedure provides the Fourier components of the surface potential in terms of an integral over the pair potential U_{pair}:

$$V_G(z) = \frac{2\pi\beta_G}{a_s}\int_0^\infty J_0(GR)\,U_{\text{pair}}\,(\sqrt{R^2+z^2})R\,dR, \tag{12}$$

where a_s is the area of the unit cell, β_G is the structure factor, and J_0 is the zero-order Bessel function. The integral is evaluated using Gaussian quadrature up to the asymptotic region where U_{pair} is simple enough to allow analytic integration.

In our attempts to reproduce the experimental data we have used five pair potentials described or referred to in the previous section.

The next term in importance is the interaction of the He atoms with the graphite surface. The V_{00} potential of He–C(0001) has been determined previously by selective adsorption measurements.[54] Since the Xe layer is located about 3.5 Å above the graphite substrate,[55] the distance of closest approach of the He atom to the substrate is fairly large, allowing V_s to be represented only by the dominating long-range term:

$$V_s(z) = -\frac{3C_3}{d^3}\zeta\left(4,\frac{z+z_0}{d}\right), \tag{13}$$

where z_0 (= 3.5 Å) is the distance from the graphite surface to the plane of the Xe layer, d (= 3.37 Å) is the interlayer distance of grapite, and $\zeta(n,x)$ [$\equiv\Sigma(j+x)^{-n}$] is the Riemann zeta function. The coefficient C_3 has a value of 170 meV/Å³.[55,56]

The V_3 contribution is calculated by the usual Axilrod–Teller–Muto expression of the tripole–dipole dispersion energy for the three atoms involved

$$E_3(\text{A,B,C}) = \nu_{\text{ABC}}\frac{1+3\cos\theta_{\text{A}}\cos\theta_{\text{B}}\cos\theta_{\text{C}}}{(r_{\text{AB}}r_{\text{BC}}r_{\text{AC}})^3}, \tag{14}$$

where the angles are the interior angles and r_{AB} is the distance between the atoms A and B, etc. The strength coefficient ν_{ABC} was calculated to be 29 eV Å⁹ by integrating numerically the upper bound polarizabilities of Ref. 57 where lower and upper bounds differ only by 2%. The summation of E_3(He,Xe,Xe) over all pairs of Xe atoms in the monolayer was carried out by Klein and Cole[58] and Chung, Holter, and Cole, [52] i.e.,

$$V_3(z) = \frac{\nu_{\text{HeXeXe}}}{a^9}\Gamma_0\,(z/a), \tag{15}$$

where a is the lattice constant of the Xe layer and $\Gamma_0(x)$ is the zero-order Fourier component given by the reduced function:

$$\Gamma_0(x) = \begin{cases} 214\exp(-4.065x), & \text{when } x\leqslant 0.6 \\ 4.144x^{-3.8} - 0.323x^{-6.78}, & \text{when } x > 0.6, \end{cases}$$

where $x = r/r_m$. Only the laterally averaged potential is retained. It contributes ~6% to the total potential at the location of the minimum of the well making it shallower.

The other triple-dipole three-body contribution, which involves He, Xe, and the graphite substrate, has been estimated by Klein, Bruch, and Cole[59] using the theory of McLachlan.[60] The form of this term is

$$V_{3s}(z) = -\frac{\pi C_{s2}}{\sqrt{3}a^2(z+2b)^4}, \tag{16}$$

where b is calculated by $z_0 - d/2$, i.e., for this system, 3.5–3.37/2 = 1.815 Å and C_{s2} is, 2710 meV Å⁶.[59] This three-body contribution is negative and smaller in magnitude than V_3.

Finally, following the procedure of Ref. 52, the thermal correction is evaluated by integrating their Eq. (28). The value of the mean-square displacement along the z direction, 0.005 29 Å at 40 K, needed in the calculation, was measured by us monitoring the effect of the temperature on the He specular intensity and using a simple Debye–Waller expression with the Beeby correction to fit the data. The integration was quite time consuming and was only included in a calculation of the bound states. Then a simple formula

$$V_t(z) = \begin{cases} f_{\text{therm}}/z^4, & \text{when } z\leqslant z_{\text{cut}} \\ 0, & \text{when } z > z_{\text{cut}} \end{cases} \tag{17}$$

was adopted and f_{therm} and z_{cut} were determined by adjusting their values until the newly produced two first bound states had exactly the same values as those calculated above. It has been checked that slight differences in higher levels have no visible effects on the calculated polar scan. The value of f_{therm} is 18.5 meV Å⁴ and z_{cut} is 7 Å for a monolayer Xe on C(0001). These values are practically independent from the choice of the pair potentials within the error limits for these which apply to the present work.

B. Close-coupling calculation

The scattering intensities for atoms diffracted by a static, periodic surface can, in principle, be exactly calculated by solving the set of close-coupled equations:

$$\left(\frac{d^2}{dz^2} + k_{G_z}^2\right)\varphi_G(z) - \frac{2m}{\hbar^2}\sum_{G'} V_{G-G'}\varphi_{G'}(z) = 0. \tag{18}$$

The numerical method used here is that of Sams and Kouri,[61] reformulated by Eastes and Secrest.[62]

For an 8.8 meV He beam, there are 19 to 23 open channels depending on the incident angle. To achieve convergence we included a total of 73 channels in the calculations. The computational time can be reduced by an order of magnitude by taking advantage of the symmetry at 0° azimuth and dropping the higher-order Fourier components of the potential when they decrease below 10^{-11} meV at intermediate z as the solution is propagated outwards. It takes a DSI-20 processor (Definicon Inc.), installed in an AST AT class microcomputer, 25 CPU hours to produce a polar scan calculation of 81 points.

C. Results and discussion

The first set of calculations was carried out by using the pair potentials described in the previous section with the standard V_s, V_3, V_{3s}, and V_t added to the zero-order Fourier component. In all the plots, the calculated and measured specularly scattered He intensity is normalized by the two parameters a and b in $I'(\theta_i) = a \cdot I(\theta_i) + b$, to have the same maximum and minimum. While some potentials are better than others, Fig. 10 shows that none of the functions gives a good fit to the experimental data. The large peak around 55° visibly shifts to the left as the bound states of V_{00} (listed in the Table VIII) become shallower.

In order to quantitatively measure the needed correction to the potential, we used a fitting parameter, f_{ATM}, which multiplies the Axilrod–Teller–Muto expression of V_3. By adjusting this parameter, we obtained the best-fit results shown in Fig. 11. The value of f_{ATM} and the corresponding bound states are listed in Table VIII.

Although the resonance features of highly corrugated system, such as the present one, are coupled and cannot be accurately predicted by the zero-order approximation, a rough assignment can still be helpful. Using the kinematic equation,

$$\mathbf{k}_i^2 - (\mathbf{K}_i + \mathbf{G}_{mn})^2 = \frac{2mE_j}{\hbar^2}, \tag{19}$$

where m is the mass of the He atom and E_j is a bound state of the laterally averaged potential, the angular positions of resonance features via low-order channels were calculated and listed in Table IX. As shown in Fig. 11(e), the 55° and 37° peaks and the minimum at 35° are possibly due to the resonances of the first bound state, E_0, via G_{10}, G_{02}, or $G_{2\text{-}2}$, and

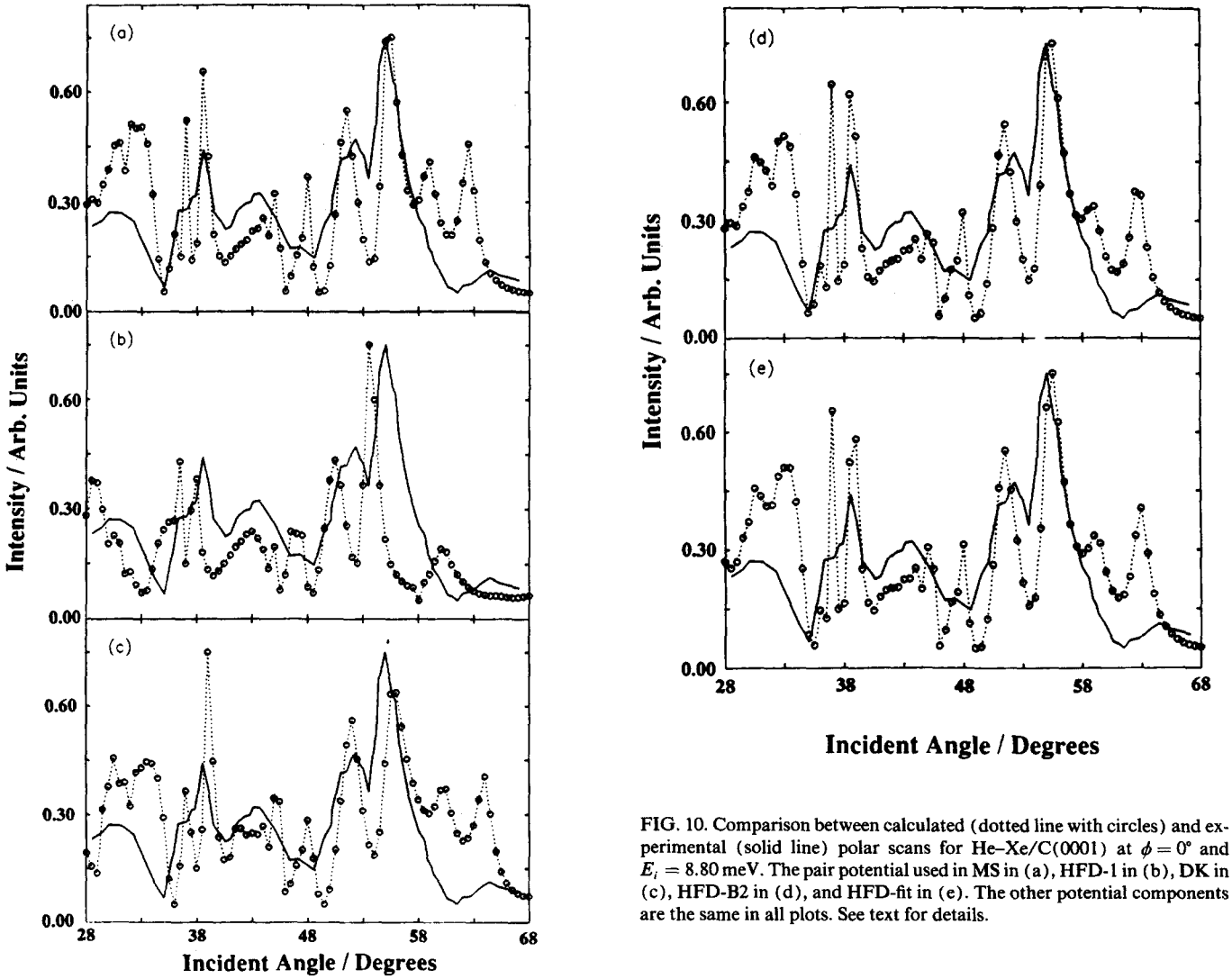

FIG. 10. Comparison between calculated (dotted line with circles) and experimental (solid line) polar scans for He–Xe/C(0001) at $\phi = 0°$ and $E_i = 8.80$ meV. The pair potential used in MS in (a), HFD-1 in (b), DK in (c), HFD-B2 in (d), and HFD-fit in (e). The other potential components are the same in all plots. See text for details.

TABLE VIII. Parameters and bound state levels of He–Xe/(0001)C potentials used in the close-coupling calculations.

Pair potential	MS[a]	HFD-1[a]	DK[b]	HFD-B[c]	HFD-fit[d]
E_{min}	−6.897	−6.579	−7.333	−7.005	−7.046
R_{min} (Å)	3.555	3.530	3.565	3.545	3.545
E_0	−4.737	−4.359	−5.082	−4.788	−4.842
E_1	−1.957	−1.644	−2.078	−1.945	−1.964
E_2	−0.650		−0.675	−0.635	−0.637
E_3	−0.165		−0.172	−0.161	−0.161
f_{ATM}	1.05	0.0	2.04	1.20	1.35
E_{min}	−6.876	−7.017	−6.899	−6.920	−6.897
R_{min} (Å)	3.555	3.515	3.580	3.550	3.555
E_0	−4.720	−4.716	−4.718	−4.718	−4.718
E_1	−1.946	−1.848	−1.857	−1.903	−1.890
E_2	−0.645	−0.595	−0.574	−0.616	−0.603
E_3	−0.163	−0.150	−0.137	−0.154	−0.149

[a] Reference 28.
[b] Reference 29.
[c] Compromise potential derived in Sec. III D 4.
[d] Best-fit potential derived in Sec. III B.

G_{11} or G_{2-1}, respectively. The shoulder at about 58° may tentatively be assigned to the second bound state, E_1, with G_{01} or G_{1-1} and G_{1-2} or G_{-12}. The E_2-character features could be the 38.5° peak and the 49° dip.

From Fig. 10 and Table IX, it is clear that the discrepancies in the neighborhood of 55° and 35° are well correlated to the different values of E_0. In the second set calculation (see Fig. 11), the first bound states are set to be the same and the effects of the different second bound states are shown at the 58° shoulder. The MS potential, although it needs the smallest correction, fails to give a good fit at the 58° shoulder, implying that the shape of the potential is not very good and does not give the correct E_1. For the HFD-1 potential, the whole V_3 term has to be eliminated, while for the DK potential, the amount of V_3 has to be doubled. The last two potentials, HFD-B2 and HFD-fit, are clearly the better potentials judged by the small correction needed and the better fit in the 58° region. It is conforting to realize that these potentials are also those that give the best fit to the transport and gas-phase scattering data.

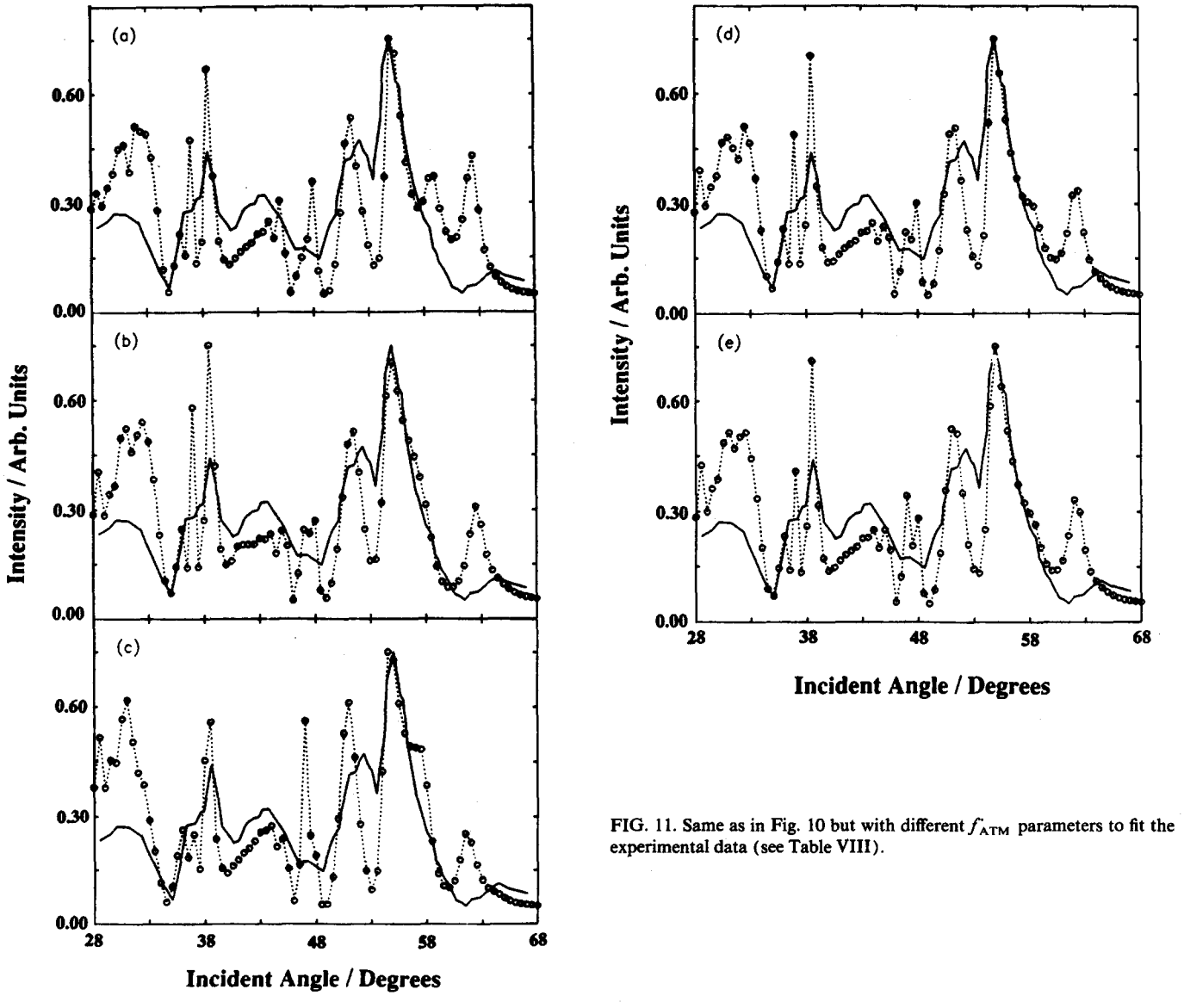

FIG. 11. Same as in Fig. 10 but with different f_{ATM} parameters to fit the experimental data (see Table VIII).

TABLE IX. Angular positions of bound-state resonance features calculated to zero order.

	G_{mn}	$E_0 = -4.72$	$E_1 = -1.89$	$E_2 = -0.60$	Threshold
G_{01}, G_{1-1}	1.687	79.1°	56.9°	49.9°	46.8°
G_{10}	1.687	55.9°	43.7°	38.5°	36.1°
G_{-12}, G_{1-2}	2.922		57.3°	48.5°	44.6°
G_{11}, G_{2-1}	2.922	34.8°	25.3°	20.7°	18.5°
G_{02}, G_{2-2}	3.375	37.1°	25.5°	19.8°	16.9°
G_{20}	3.375	24.7°	16.3°	12.2°	10.3°

To show the sensitivity of the resonance features to the bound states, we made calculations with the first bound state 1% higher (4.77 meV) and 1% lower (4.67 meV) than the best-fit bound state (4.72 meV) with f_{ATM} set at 1.2 and 1.5 as shown in Figs. 12(a) and 12(b), respectively. Concentrating in the 35°–38° region and the main peak at 55°, the significance of the differences from the experimental data in the two figures is easily evaluated by comparison with Fig. 11(e). It appears that the bound-state energies can be determined with $\pm$ 1% uncertainty for this highly corrugated ($\sim$0.9 Å) system through the close-coupling calculations.

As mentioned in Sec. II, the width of the velocity distribution of the He beam is 2% at FWHM while the graphite and layer imperfections cause the specular peak to be 1° wider than the incident beam. These factors broaden considerably the resonance features in the measured polar scan. In order to make a better comparison between the calculation and the experiment, two more calculations were made with the incident energies $\pm$ 2% from the central energy. Each of the three calculations was corrected with a Debye–Waller factor which included the Beeby correction to account for thermal effects. All three calculations were then averaged with a weight factor of 2 added to the one obtained by using the central energy. Finally, the difference in width between specular and primary beam was accounted for by averaging over three contiguously calculated points (0.5° apart in the incident angle) with the intensity of the central point being doubled. The result of this averaging procedure using the HFD-fit potential is shown in Fig. 13. The fit is quite good except that in the regions around 47°, 52°, and 62°. These discrepancies could not be eliminated by any of the corrections to the potential which we have tried and occur in the regions where no profound resonance features are predicted by the zero-order approximation. The good agreement for all the assigned features and their well-understood behavior upon changing the bound states convinced us that the HFD-fit pair potential is quite accurate and that in order to obtain the proper bound states a small correction (to amount to $-$ 2.6% in overall well depth) in some of the other terms in volved in V_{00} is needed.

First of all, we checked for possible errors in the lattice constant. Depending on the coverage and the temperature, the lattice constant of the Xe layer can vary from 4.28 to 4.32 Å under our experimental conditions. We, as mentioned in the Sec. II, tried to prepare the layer for this polar scan with caution to ensure that full coverage was reached. The observed value of 4.30 is the average of five diffraction scans at different incident angles. In Fig. 14(a), we show the calculated polar scan with a lattice constant of 4.32 Å but using a lower f_{ATM} (1.24) to retain the same bound-state values. Similarly, for a lattice constant of 4.28 Å, 1.45 was used for f_{ATM} and the result plotted in Fig. 14(b). Both figures dis-

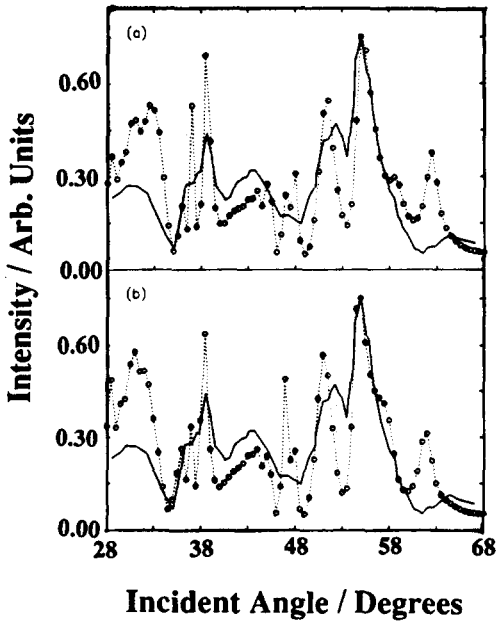

FIG. 12. Same as in Fig. 10(e) but with (a) $f_{ATM} = 1.2$ and (b) $f_{ATM} = 1.5$.

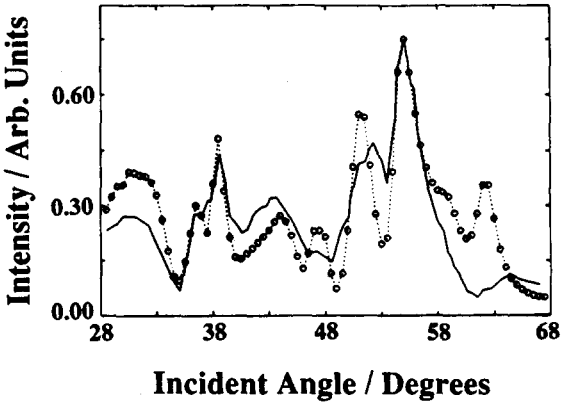

FIG. 13. Comparison between (*averaged*) calculated result (dotted line with circles) and experimental result (solid line) for the HFD-fit pair potential with $f_{ATM} = 1.35$.

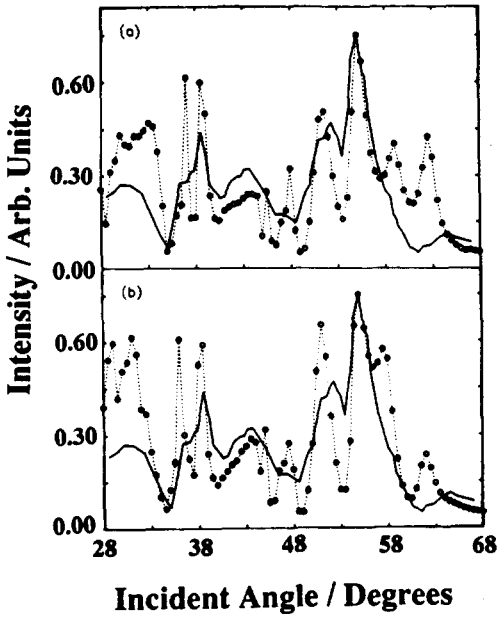

FIG. 14. Comparison between (*averaged*) calculated (dotted line with circles) and experimental (solid line) polar scans of He–Xe/C(0001) for $\phi = 0°$ and $E_i = 8.80$ meV for variations of the HFD-fit pair potential. (a) $A = 4.32$ Å and $f_{\mathrm{ATM}} = 1.24$ and (b) $A = 4.28$ Å and $f_{\mathrm{ATM}} = 1.45$.

play larger discrepancies in the shape of the intensity oscillations than those seen in Fig. 11(e), where the lattice constant is 4.30 Å. This can be taken as a further confirmation that there are no errors due to an incorrect lattice constant.

The contribution from each component of the laterally averaged potential is then plotted in Fig. 15. The last two terms, V_{3s} and V_t, contribute only 1.5% and 0.8%, respectively, at the minimum of the total potential. The errors in these terms would be too small to explain the 2.6% correction. We conclude our discussion debating the remaining possibilities. First of all, if V_2 and V_3 are assumed to be correct, and therefore f_{ATM} is kept fixed at 1, a good fit can also be achieved by lowering the graphite long-range attraction coefficient, C_3, from 170 meV Å^3 to 145 meV Å^3 [see Fig. 16, which should be compared with Fig. 11(e)]. This seems to be a rather large correction in view of the commonly assumed accuracy of the theoretical calculations that lead to the value indicated above.

On the other hand, as suggested in Ref. 14(a), the possibility exists that the commonly accepted C_3 value be correct but that its use in the region of interest (approximately 7 Å) not be justified (i.e., the shape of the potential is quite different from the long-range form). Further theoretical activity in this area to establish these long-range interactions within narrower limits would be useful. The second possibility is that the neglected higher terms of the three-body HeXeXe potential would generate, if included, a further repulsive contribution which would amount to 20–30% of the ATM term. We have estimated the higher multipole contributions to the three-body interaction, namely *DDQ*, *QDD*, *DQQ*, *QDQ*, *QQQ*, *DDO*, and *ODD*. All but *QDQ* lead to a further repulsive contribution to the overlayer potential, the *DDQ* term being by far the largest. The net contribution of these terms is a repulsive shift in the lowest bound state amounting to ~20% of the shift due to the ATM term. This is similar, in relative magnitude, as the contribution to the cohesive energy of Xe and Kr crystals. There it is found that the higher multipole contributions to the three-body correction is largely cancelled by corrections coming from higher-order perturbation theory. We have not estimated those terms for the overlayer potential but it is likely that a similar cancellation occurs in this case.

The third possibility is that of an error in the two-body potential. As discussed in Sec. II B, we estimate the maximum error in the well depth to about 1.6%. Therefore, while a change of this type would go a long way towards improving agreement with experiment, it could not by itself bring the bound-state energies to the level where we expect them to be.

Of course a reduced but simultaneous occurrence of

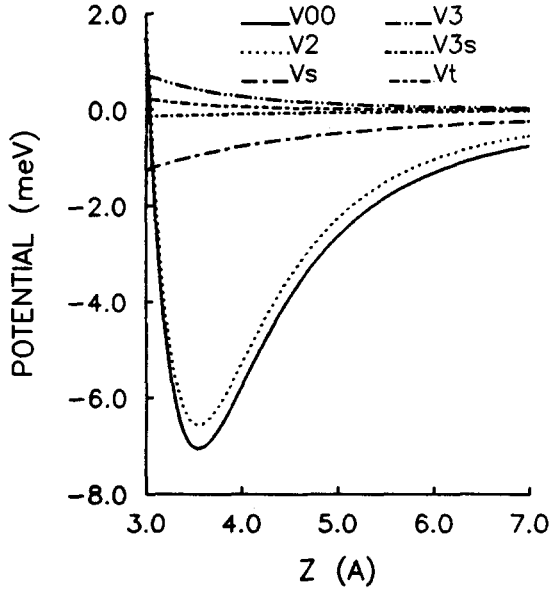

FIG. 15. The laterally averaged He–Xe/C(0001) potential and its different components. The total potential, V_{00} (solid line), the pairwise sum, V_2 (dotted line), V_s (dashed line), V_3 (loose dashed line), V_{3s} (dot–dashed line), and V_t (dot–dot–dashed line).

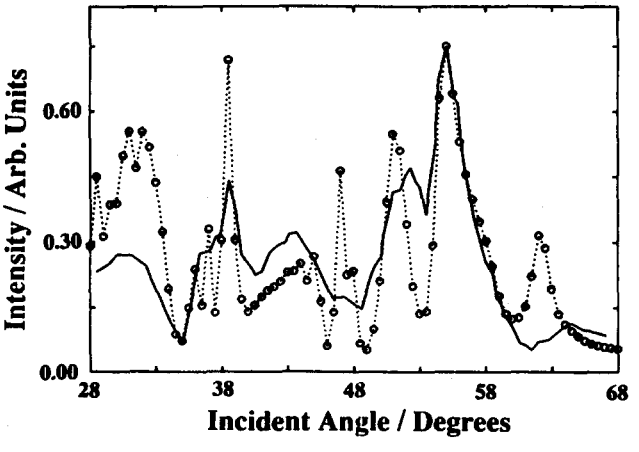

FIG. 16. Same as in Fig. 10(e) but with C_{3gr} changed from 170 to 145 meV Å^3 to fit the experimental data.

both errors could instead produce good agreement with our experimental results.

In summary, in this paper we have introduced a very accurate He–Xe two-body potential that represents a substantial improvement over the present situation, and we have shown that the use of close-coupling calculations, combined with a good knowledge of the interactions, allows for reaching good agreement between calculated and measured intensities in low-energy atom-surface "total" scattering experiments, provided that, in agreement with previous work[16(b),18] the triple-dipole ATM three-body interaction is taken into account.

We have further established that if further progress is to be made on our knowledge of three-body interactions in He–noble-gas mixtures by means of He–overlayer scattering experiments we need to do the following: (a) establish the two-body potential well depth to an accuracy of better than 1%; (b) establish the long-range He–bare-crystal interaction to an accuracy of 5% or better at all distances below 10 Å; and (c) substantially improve the efficiency of the computational code (or the computational tools) so that a fully averaged *automatic* fitting procedure could be set up in which the gas–overlayer scattering data would be used directly (together with the two-body properties) in the simultaneous determination of the best two- and three-body interactions. Unless at least two of these conditions are met, future workers in this area should be prepared to be disappointed.

ACKNOWLEDGMENTS

One of us (J.-C.R.-S.) would like to acknowledge a scholarship from Consejo Nacional de Ciencia y Tecnológia (Mexico) and La Universidad Autonoma de Puebla (Mexico) for granting a leave to study abroad. It is a pleasure to thank P. A. Rowntree for useful discussions and assistance during the course of this work. Useful discussions with M. L. Klein, M. W. Cole, M. Keil, L. Danielson, and P. Dunlop are also gratefully acknowledged.

[1]A. Thomy and X. Duval, J. Chim Phys. **66**, 1966 (1969); **67**, 1101 (170); M. Bretz and J. G. Dash, Phys. Rev. Lett. **27**, 647 (1971); M. Bretz, J. G. Dash, D. C. Hickernell, E.O. McLean, and O. E. Vilches, Phys. Rev. **8**, 1589 (1973); H. K. Kim, Y. P. Feng, Q. M. Zhang, and M. H. W. Chan, Phys. Rev. B **37**, 3511 (1988).

[2]Lander and J. Morrison, Surf. Sci. **6**, 1 (1967); J. Suzanne, J. P. Coulomb, and M. Bienfait, *ibid.* **40**, 414 (1973); **44**, 141 (1974); **47**, 204 (1975); J. K. Kjems, L. Passell, H. Taub, and J. G. Dash, Phys. Rev. Lett. **32**, 724 (1974); Phys. Rev. B **13**, 1146 (1976); J. A. Venables, H. J. Kramer, and G. L. Price, Surf. Sci. **55**, 373 (1976); **57**, 782 (1976); P. M. Horn, R. J. Birgeneau, P. Heiney, and E. M. Hammonds, Phys. Rev. Let. **41**, 961 (1978); T. H. Ellis, S. Iannotta, G. Scoles, and U. Valbusa, Phys. Rev. B **24**, 2307 (1981).

[3]H. H. Richardson and G. E. Ewing, J. Phys. Chem. **91**, 5833 (1987); H. C. Chang, H. H. Richardson, and G. E. Ewing, J. Chem. Phys. **89**, 7561 (1988).

[4]S. C. Fain, Jr., M. F. Toney, and R. D. Diehl, in *Proceedings of the 9th International Vacuum Congress and 5th International Conference on Solid Surfaces*, edited by J. L. de Segovia (Imprenta Moderna, Madrid, 1983).

[5]A. Ignatiev and T. N. Rhodin, Phys. Rev. B **8**, 893 (1973); M. F. Toney and S. C. Fain, Jr., *ibid.* **36**, 1248 (1987); J. W. Osen and S. C. Fain, Jr., *ibid.* **36**, 4074 (1987).

[6]H. J. Taub, K. Carneiro, J. K. Kjems, L. Passell, and J. P. McTague, Phys. Rev. B **16**, 4551 (1977); Y. P. Joshi, D. J. Tildesley, J. S. Ayres, and R. K. Thomas, Mol. Phys. **65**, 991 (1988).

[7]H. Hong, C. J. Peters, A. Mak, R. J. Birgenau, P. M. Horn, and H. Suematsu, Phys. Rev. B **36**, 7311 (1987).

[8](a) T. H. Ellis, G. Scoles, and U. Valbusa, Surf. Sci. **118**, 1251 (1982); (b) T. H. Ellis, G. Scoles and U. Valbusa, Chem. Phys. Lett. **94**, 247 (1983); (c) T. H. Ellis, G. Scoles, U. Valbusa, H. Jónsson, and J. H. Weare, Surf. Sci. **155**, 499 (1985); (d) H. Jónsson, J. H. Weare, T. H. Ellis, and G. Scoles, *ibid.* **180**, 353 (1987); (e) J. C. Ruiz-Suárez, M. L. Klein, M. A. Moller, P. Rowntree, G. Scoles, and J. Xu, Phys. Rev. Lett. **61**, 710 (1988); (f) K. Kern, P. Zeppenfeld, R. David, and G. Comsa, *ibid.* **59**, 79 (1987); (g) K. D. Gibson, S. J. Sibener, B. M. Hall, D. L. Mills, and J. E. Black, J. Chem. Phys. **83**, 4256 (1985); (h) J. Z. Larese, W. Y. Leung, D. R. Frankl, N. Holter, S. Chung, and M. W. Cole, Phys. Rev. Lett. **54**, 2533 (1985).

[9]S. K. Satija, M. Sutton, R. J. Birgenau, H. Hong, L. Passell, and J. P. Wicksted, Phys. Rev. B **35**, 2064 (1987).

[10]J. G. Dash, Phys. Rev. B **15**, 3136 (1977).

[11]R. Pandit, M. Schick, and M. Wortis, Phys. Rev. B **26**, 5112 (1982).

[12]J. A. Barker and P. J. Auerbach, Surf. Sci. Rep. **4**, 1 (1985).

[13]G. Ihm, M. W. Cole, F. Toigo, and G. Scoles, J. Chem. Phys. **87**, 3995 (1987).

[14](a) H. Y. Kim and M. W. Cole, Phys. Rev. B **35**, 3990 (1987); (b) S. Gauber, J. R. Klein, and M. W. Cole, *ibid.* **27**, 1314 (1983); (c) J. R. Klein, L. W. Bruch, and M. W. Cole, Surf. Sci. **173**, 555 (1986).

[15](a) G. Bracco, P. Cantini, E. Cavanna, R. Tatarek, and A. Glachant, Surf. Sci. **136**, 169 (1984); (b) J. M. Hutson and C. Schwartz, J. Chem. Phys. **79**, 5179 (1983).

[16](a) H. Jónsson and J. H. Weare, Faraday Discuss. Chem. Soc. **80**, 29 (1985); (b) Phys. Rev. Lett. **57**, 412 (1986); (c) C. Chung, A. Kara, and D. R. Frankl, Surf. Sci. **171**, 45 (1986); (d) J. C. Ruiz-Suárez, G. Scoles, and H. Jónsson, Chem. Phys. Lett. **129**, 139 (1986).

[17]K. Kern, P. Zeppenfeld, R. David, and G. Comsa, *Structure of Solid Surfaces II*, edited by J. F. v.d. Veen and M. A. v. Hove (Springer, Heildelberg, 1988), p. 488; K. Kern, P. Zeppenfeld, R. David, and G. Cosma, J. Electron Spectrosc. Relat. Phenom. **44**, 215 (1987); K. Kern, P. Zeppenfeld, R. David, and G. Comsa, J. Vac. Sci. Tech. A **6**, 639 (1988).

[18]K. D. Gibson and S. J. Sibener, J. Chem. Phys. **88**, 7862 (1988); **88**, 7893 (1988); K. D. Gibson, C. Cerjan, J. C. Light, and S. J. Sibener, *ibid.* **88**, 7911 (1988).

[19]L. Danielson, J. C. Ruiz, C. Schwartz, G. Scoles, and J. M. Hutson, Faraday Discussions Chem. Soc. **80**, 47 (1985).

[20]G. Caracciolo, S. Iannotta, G. Scoles, and U. Valbusa, J. Chem. Phys. **72**, 4491 (1980).

[21]U. Buck, G. Hoffmann, J. Kesper, D. Otten, and M. Winter, Chem. Phys. **126**, 159 (1988).

[22]U. Buck, in *Atomic and Molecular Beam Methods*, edited by G. Scoles (Oxford University Press, New York, 1988), Chap. 20.

[23]M. Keil, L. J. Danielson, U. Buck, J. Schleusener, F. Huisken, and T. Dingle J. Chem. Phys. **89**, 2866 (1988).

[24]P. S. Arora, H. L. Robjohns, and P. J. Dunlop, Physica **95A**, 561 (1979).

[25]A. Kumar and W. J. Meath, Mol. Phys. **54**, 823 (1985).

[26]C. Douketis, G. Scoles, S. Marchetti, M. Zen, and A. J. Thakkar, J. Chem. Phys. **76**, 3057 (1982).

[27]B. Najafi, E. A. Mason, and J. Kestin, Physica **119A**, 387 (1983).

[28]K. M. Smith, A. M. Rulis, G. Scoles, R. A. Aziz, and V. Nain, J. Chem. Phys. **67**, 152 (1977).

[29]L. J. Danielson and M. Keil, J. Chem. Phys. **88**, 851 (1988).

[30]T. S. Storvick and E. A. Mason, J. Chem. Phys. **45**, 3752 (1966).

[31]S. C. Saxena and R. K. Joshi, Physica **29**, 870 (1963).

[32]R. A. Aziz, F. R. W. McCourt, and C. C. K. Wong, Mol. Phys. **61**, 1487 (1987).

[33]R. A. Aziz and M. J. Slaman, Mol. Phys. **57**, 825 (1986).

[34]E. Vogel, Ber. Bunsenges. Phys. Chem. **88**, 997 (1984).

[35]J. Kestin, S. T. Ro, and W. A. Wakeham, J. Chem. Phys. **56**, 4086 (1972).

[36]J. Kestin, K. Knierim, E. A. Mason, B. Najafi, S. T. Ro, and N. Waldham, J. Phys. Chem. Ref. Data **13**, 229 (1984).

[37]T. R. Marrero and E. A. Mason, J. Phys. Chem. Ref. Data **1**, 3 (1972).

[38]P. J. Dunlop (private communication).

[39]W. L. Taylor and D. Cain, High Temp. High Press. **15**, 433 (1983).

[40]R. J. J. van Heijningen, J. P. Harpe, and J. J. M. Beenakker, Physica **38**, 1 (1968).

[41]P. J. Dunlop (private communication).

[42]R. A. Aziz and M. J. Slaman, Chem. Eng. Commun. **78**, 153 (1989).

[43]R. D. Trengove, H. L. Robjohns, T. N. Bell, M. L. Martin, and P. J. Dunlop, Physica **108A**, 488 (1981).

[44]W. L. Taylor (private communication).
[45]J. Brewer, U. S. Air Force Office of Scientific Research, Arlington, Virginia, Report No. 67-2795 (1967).
[46]F. H. Kate, Jr. and R. L. Robinson, Jr., J. Chem. Thermodyn. **5**, 259 (1973).
[47]H. H. Chen, C. C. Lim, and R. A. Aziz, J. Chem. Thermodyn. **10**, 649 (1978).
[48]C. Tessier, A. Terlain, and Y. Larher, Physica **113A**, 286 (1982).
[49]P. K. Rol, as cited in R. A. Aziz, *Inert Gasses*, Springer Series in Chemical Physics, Vol. 34, edited by M. L. Klein (Springer, Berlin, 1984).
[50]R. A. Aziz and H. H. Chen, J. Chem. Phys. **67**, 5719 (1977).
[51]J. M. Standard and P. R. Certain, J. Chem. Phys. **83**, 3002 (1985).
[52]S. Chung, N. Holter, and M. W. Cole, Phys. Rev. B **31**, 6660 (1985).
[53]W. A. Steele, Surf. Sci. **36**, 317 (1973).
[54]J. C. Ruiz, G. Scoles, and H. Jónsson, Chem. Phys. Lett. **129**, 139 (1986).
[55]T. H. Ellis, S. Iannotta, G. Scoles, and U. Valbusa, Phys. Rev. B **24**, 2307 (1981).
[56]G. Vidali, M. W. Cole, and G. Schwartz, Surf. Sci. **87**, L273 (1979).
[57]K. T. Tang, J. M. Norbeck, and P. R. Certain, J. Chem. Phys. **64**, 3063 (1976).
[58]J. R. Klein and M. W. Cole, Surf. Sci. **134**, 722 (1983).
[59]J. R. Klein, L. W. Bruch, and M. W. Cole, Surf. Sci. **173**, 555 (1986).
[60]A. D. McLachlan, Mol. Phys. **7**, 381 (1964).
[61]W. N. Sams and D. J. Kouri, J. Chem. Phys. **51**, 4809 (1969); **52**, 4144 (1970).
[62]W. Eastes and D. Secrest, J. Chem. Phys. **56**, 640 (1972).